THE JOURNAL OF PHYSICAL CHEMISTRY C
A JOURNAL OF THE AMERICAN CHEMICAL SOCIETY

pubs.acs.org/JPCC

Article

Semidefective Graphene/h-BN In-Plane Heterostructures: Enhancing Interface Thermal Conductance by Topological Defects

Xin Wu and Qiang Han*

Cite This: J. Phys. Chem. C 2021, 125, 2748–2760

Read Online

ACCESS | Metrics & More | Article Recommendations

ABSTRACT: Two-dimensional (2D) in-plane heterostructures, whose interface thermal conductance (ITC) plays a crucial role in the thermal performance of nanostructured materials, will undoubtedly become the focus of the next-generation nanoelectronic devices. In this work, the semidefective graphene/hexagonal boron nitride in-plane heterostructures were innovatively proposed based on topological defects, and the thermal conductance across its interface was studied by molecular dynamics simulations. Surprisingly, the topological defects of a certain component in the heterostructure can significantly improve its ITC without changing the interfacial structure, and it is expected to be controlled by the defective concentration and the average temperature of the system. In particular, based on the different defective objects, the improvement of the ITC exhibits a radically different trend as the defective concentration increases. After the phonon activities were captured to explore the underlying physical mechanisms, it is found that the phonon coupling on both sides of the interface and the phonon localization effect of the heterostructure are two pivotal factors that determine the ITC of the heterostructure. The discovery of these results suggests a new path forward for improving or even controlling the ITC of the 2D in-plane heterostructures.

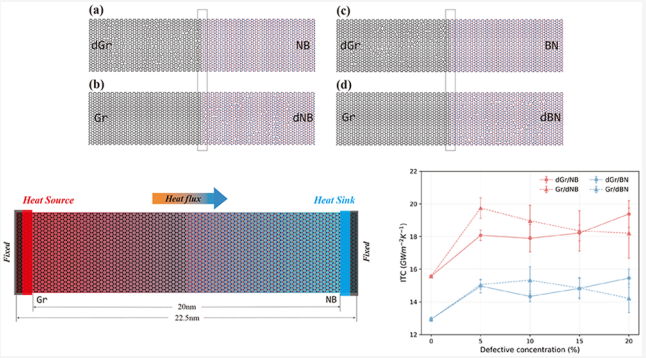

INTRODUCTION

Since the 21st century, a class of two-dimensional (2D) materials, such as graphene (Gr) and hexagonal boron nitride (h-BN), have been widely hailed by many researchers for their exceptional physical, chemical, and mechanical properties, and have therefore become promising candidates for advanced device applications such as next-generation nanoelectronic devices.[1−4] In particular, the heterostructures (including in-plane stitching and out-of-plane stacking) composed of these materials not only exert the excellent characteristics of their constituent elements, but also bring additional adjustability in terms of electrical and thermal response.[5−7] In the technological field that keeps pace with the development of the above-mentioned materials, the microelectronics technology, which is leading the third technological revolution, continues to live up to the legend of "Moore's Law". Unfortunately, however, heat transfer, a basic energy transport mechanism which is of equal importance to electric conduction, has never received the attention it deserves.

In recent years, based on the inspiration of the phonon, which is analogue of the electron, thermal elements such as thermal diodes and thermal transistors have been proposed to realize the transfer and control of heat in nanosystems.[8−11] Surprisingly, the rise of 2D heterostructures has brought unlimited possibilities for heat transfer and control from the perspective of structural design,[12−24] which is of great significance to the development of phononics. Chen et al.[12] successfully discovered the negative differential thermal resistance behaviors caused by the phonon resonance effect and lattice vibration mismatch in the graphene/hexagonal boron nitride in-plane heterostructure (Gr/h-BN). Wang et al.[13] used lateral phonon confinement to achieve thermal rectification on asymmetric graphene nanoribbons by means of structural design, which has a breakthrough significance for controlling heat flow. The results of research on the control of the thermal transport properties of 2D heterostructures through defect engineering[14−16] are also getting abundant. In addition, substrate engineering[17−20,23,24] and strain engineering,[21,22] as effective means for the property regulation of nanomaterials also play an indispensable role in the thermal management and thermal design of 2D materials and their heterostructures.

Received: November 18, 2020
Revised: January 12, 2021
Published: January 21, 2021

https://dx.doi.org/10.1021/acs.jpcc.0c10387
J. Phys. Chem. C 2021, 125, 2748−2760

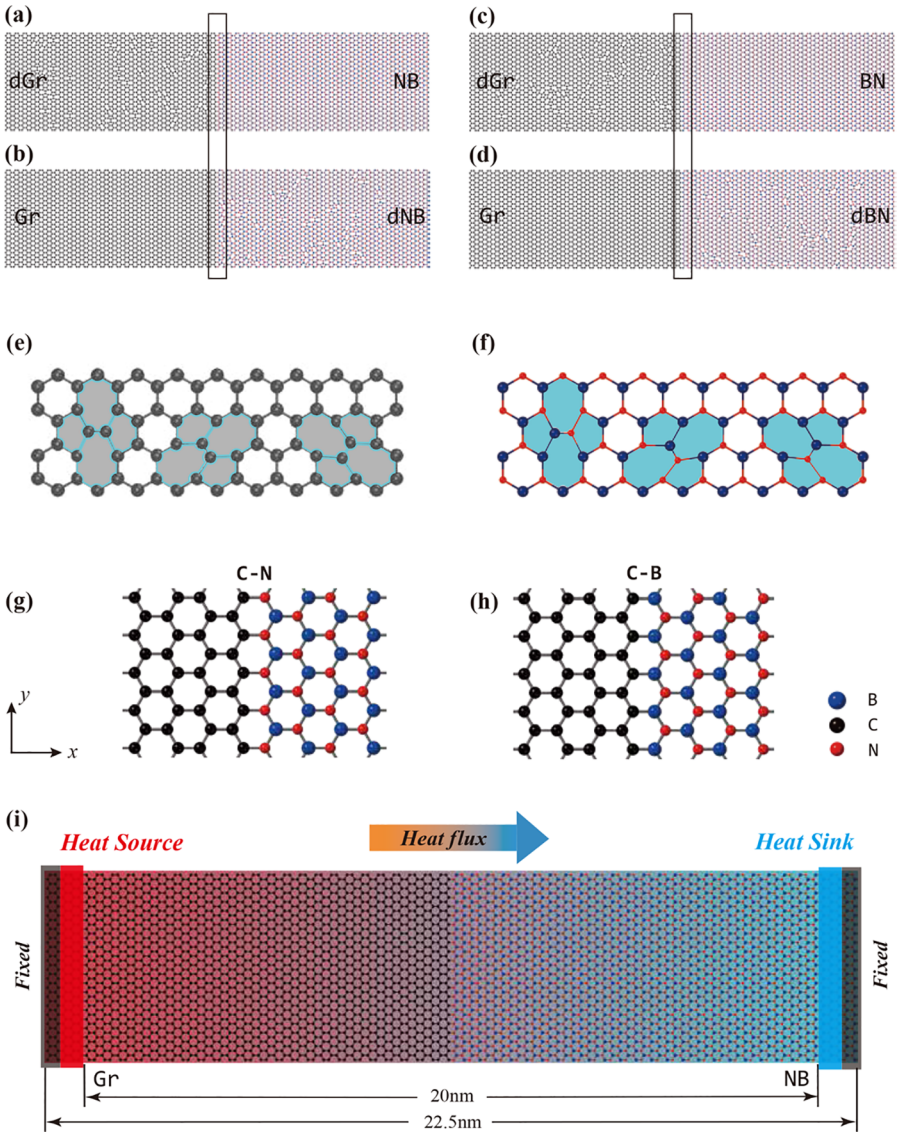

Figure 1. Schematic diagram of the semidefective Gr/h-BN in-plane heterostructures with an in-plane size of 22.5 nm × 5 nm (taking 20% defective concentration as an example). There are (a) defective graphene/hexagonal boron nitride (dGr/NB) and (b) graphene/defective hexagonal boron nitride (Gr/dNB) heterostructures with C−N interface, and (c) defective graphene/hexagonal boron nitride (dGr/BN) and (d) graphene/defective hexagonal boron nitride heterostructures (Gr/dBN) with C−B interface. Panels (e) and (f) are the spatial structures of topological defects in Gr and h-BN, respectively. The top view of the 2D in-plane Gr/h-BN heterostructure atomic model including (g) C−N interface and (h) C−B interface. (i) The sketch of in-plane Gr/h-BN heterostructure used to illustrate the MD simulation. The two ends of the heterostructure in the *x*-direction each have a fixed layer with a width of 4.3 Å, and inward is a thermal bath layer with a width of 8.6 Å, which contains a heat source and heat sink, thereby generating a stable heat flux along the *x*-direction of the structure.

Benefiting from the rapid development of material synthesis technology, the preparation of 2D heterostructures, is no longer an unrealistic fantasy.[25−32] Ci et al.[25] have completed the synthesis and characterization of large-area atomic layers of hybridized boron nitride and graphene domains, which is a revelation for the preparation of Gr/h-BN through doping. Relying on the lattice constant difference of less than 2%, Gr and h-BN have unique advantages in synthesizing heterostructures.[26] So far, the Gr/h-BN with a clear interface and complete structure has been successfully synthesized by chemical vapor deposition (CVD),[27] epitaxial growth,[28] and chemical conversion method.[29] At the same time, its better tunability gives Gr/h-BN broad application prospects as thermal management materials, which also brings considerable research value.[20,32−37] For heterostructures, interface issues are often very worthy of attention, and of course, it is no exception in the field of heat transfer. In particular, Liu et al.[32] enhanced the heat transfer capability of the Gr/h-BN interface through atomic doping and interface topology optimization. Liu et al.[33] reported that topological defects at the interface of Gr/h-BN unexpectedly increase the interface thermal conductance (ITC), which is in sharp contrast to the common notion that interface defects promote phonon scattering.

In this study, a class of semidefective Gr/h-BN was proposed, and topological defects were innovatively applied to a certain initial component, which improves the thermal conductance across the interface without changing the interfacial structure. Through nonequilibrium molecular dynamics simulations, it was found that in the semidefective Gr/h-BN, the ITC will increase significantly with the increase

https://dx.doi.org/10.1021/acs.jpcc.0c10387
J. Phys. Chem. C 2021, 125, 2748−2760

of the defective concentration. Meanwhile, there is no obvious thermal rectification phenomenon, and the effect of temperature on the ITC of the heterostructure was also studied. In addition, from the perspective of phonons, the phonon density of state in the frequency domain and the phonon participation rate reflecting the phonon characteristics reveal the interface heat transfer mechanism contained in the above results.

MODELS AND METHODS

Models of Semidefective Gr/h-BN In-Plane Heterostructures. In order to model 2D Gr/h-BN in-plane heterostructures, determining the bonding configuration of atoms at the interface is a top priority. The in-plane Gr/h-BN interface is more inclined to form zigzag stitching edges, both experimentally and theoretically, which are more favorable in energy than armchair-shaped edges.[27,38,39] There are two possibilities for the interface with the zigzag stitching edges, namely, the C−N and C−B bonding configurations shown in Figure 1g−h. To this end, the heterostructures with the C−N bonding interface are referred to as Gr/NB and those with the C−B bonding interface as Gr/BN in this study. At the same time, whether it is Gr or h-BN, the defect modification introducing topological defects to transform it into defective state, from theory to experiment, has attracted widespread attention from the academia.[40−43]

Inspired by this, an algorithm specifically designed for modeling was developed, which can construct semidefective Gr/h-BN in-plane heterostructures with stochastically distributed topological defects with specified concentrations. The topological defects, also called 5−7−7−5 defects, are introduced by 90° in-plane rotation of a certain chemical bond and two bonded atoms, as shown in Figure 1e−f. In regular hexagonal structures such as Gr and h-BN, there are three types of chemical bonds with different orientations, which brings randomness of defect orientation. Insofar, the stochastic setting of defect location and orientation determines the randomness of defect distribution. Admittedly, it is a sound way to avoid the influence of the particularity of the model on the calculation results. Because of the pairwise combination of different defective objects and heterogeneous interfaces, there are four different semidefective Gr/h-BN in-plane heterostructures; see Figure 1a−d for an illustration. The dimensions of all models used for simulation along the x (armchair direction) and y (zigzag direction) are 22.5 nm and 5 nm, respectively, and the total number of atoms is 4368.

MD Simulation Details. All the molecular dynamics (MD) simulations in this study were carried out by the efficient graphics processing units molecular dynamics (GPUMD) code,[44,45] which implements massively parallel classical MD calculations on the GPU architecture. It greatly improves the computational efficiency while avoiding the errors of the commonly used large-scale atom/molecule massively parallel simulator (LAMMPS) package in the heat flux formula under multibody potential.[46−49] Optimized Tersoff potential by Kinaci et al.,[50] a reliable and accurate interatomic potential for intrinsic and extrinsic phonon scattering, was used to describe the covalent interaction among B, C, and N atoms.[20,32−37] Moreover, a time step of 0.5 fs was selected throughout the simulation process to ensure good system stability and energy conservation.

In this paper, the nonequilibrium molecular dynamics (NEMD) method was used to study the ITC of semidefective Gr/h-BN heterostructures, which is a universal and effective method to study the interfacial heat transfer. As shown in Figure 1i, fixed boundary conditions with a width of 4.3 Å were applied at both ends of the x direction, whereas periodic boundary conditions were applied in the y direction. Free boundary conditions were applied in the out-of-plane direction to satisfy the unrestricted out-of-plane motion of atoms. First, at the target temperature, each initial structure will undergo a relaxation for 2 ns (4 million time steps) under the NVT ensemble controlled by the Berendsen thermostat. Next, switching from the global thermostat to the local thermostat achieves a hot and cold bath. To this end, heat source and heat sink areas with a width of 8.6 Å were respectively defined inward from the fixed layer at both ends of the structure. Through the Langevin local thermostat, the temperatures of $T_h = T_0(1 + \Delta)$ and $T_c = T_0(1 - \Delta)$ were applied to the heat source and heat sink area respectively to generate nonequilibrium heat flux J, and the duration is 6 ns (12 million time steps). Among them, T_0 represents the average temperature of the system, and Δ is the normalized temperature difference between the heat source and the heat sink. In the Langevin thermostat,[51] the motion equation of particles in the constant temperature region is

$$\frac{d\vec{r}_i}{dt} = \frac{\vec{p}_i}{m_i}$$
$$\frac{d\vec{p}_i}{dt} = \vec{F}_i - \frac{\vec{p}_i}{\tau} + \vec{f}_i \quad (1)$$

where $\vec{r}_i$, $\vec{p}_i$, m_i,$\vec{F}_i$ are the location, momentum, mass and force of atom i, respectively; $\vec{f}_i$ is the stochastic force with a variation determined by the fluctuation−dissipation relation to achieve the NVT ensemble distribution at the target temperature; τ is time parameter, which determines the strength of the thermostat for temperature control. In this study, τ is 0.05 ps, or 100 time steps, which is small enough to achieve proper temperature control.

Because of the total energy conservation of the system, the reduced energy of the heat source and the increased energy of the heat sink are almost equal under the same time. We define the heat flux J along the x direction as

$$J = \frac{|dE/dt|}{A} \quad (2)$$

Among them, $|dE/dt|$ represents the energy exchange rate between the heat source and the heat sink under nonequilibrium steady state. A is the cross-sectional area of the interface perpendicular to the direction of heat flux, which is calculated by the product of the thickness of the monolayer heterostructure, about 0.335 nm, and the width of it. Next, the sample was divided equally into 46 slabs along the heat flux direction, and the temperature in each slab was calculated based on the energy equalization theorem

$$T = \frac{1}{3Nk_B}\sum_{i=1}^{N} m_i v_i^2 \quad (3)$$

where N is the number of atoms in each slab, k_B is the Boltzmann constant, m_i and v_i are the mass and velocity of the atom i. Under the nonequilibrium steady state, due to the existence of the interface, there will appear discontinuous temperature distributions between both sides. The time average temperature jump ΔT can be obtained by linear

https://dx.doi.org/10.1021/acs.jpcc.0c10387
J. Phys. Chem. C 2021, 125, 2748−2760

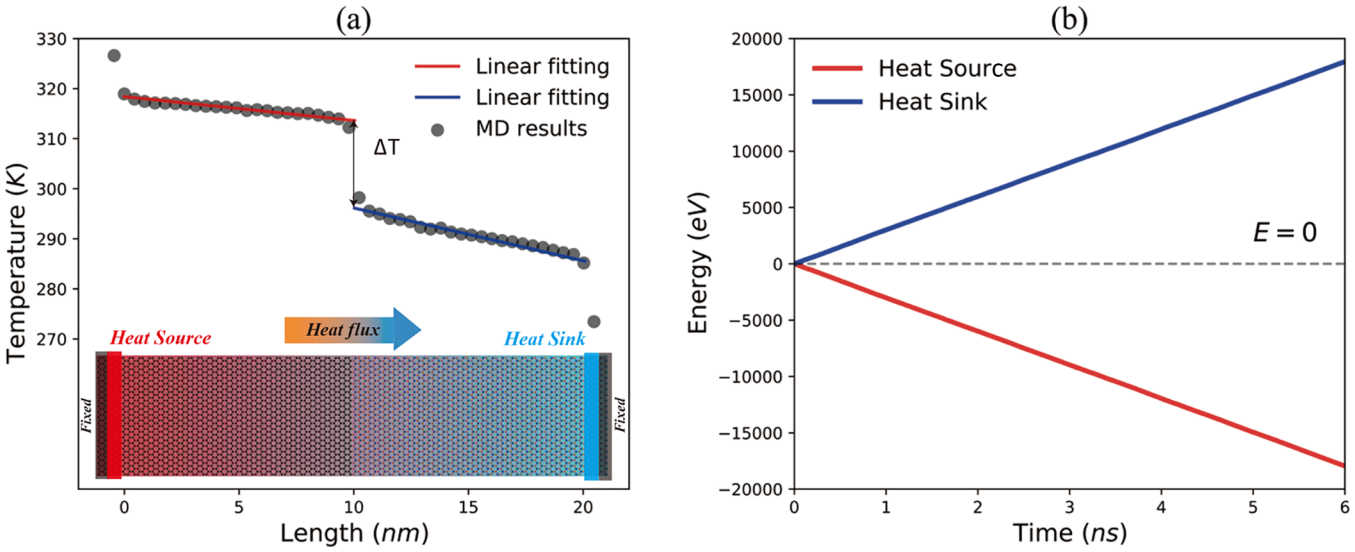

Figure 2. (a) Under the temperature configuration of T_0 = 300 K, Δ = 0.1, the typical steady-state temperature profile of the pristine Gr/NB in-plane heterostructure calculated by the NEMD method. The heat flux is from the Gr domain to the h-BN domain, where a significant Kapitza temperature drop is found at its interface. Furthermore, the temperature jump ΔT at the interface can be determined by linear fitting by the temperature data. (b) Under the Langevin thermostat, the steady-state cumulative energy of the heat source located in the Gr domain and the heat sink of the h-BN domain varies with simulation time. It should be noted that the approximate symmetry of the heat source and heat sink curves with respect to the dashed line E = 0 means that the total energy of the system is conserved.

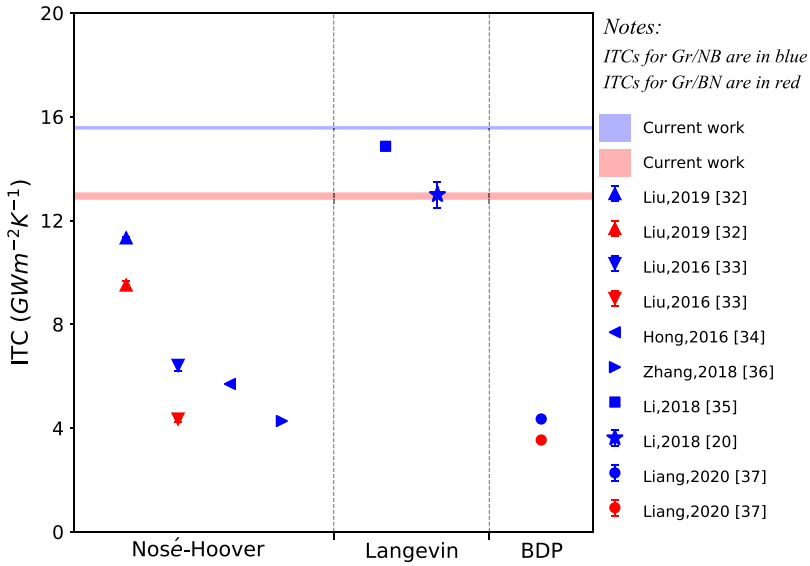

Figure 3. Under similar models and temperature conditions, the influence of different thermostats on the ITC of pristine Gr/NB (blue markers) and Gr/BN (red markers). This includes seven groups of studies using three types of thermostats: Nosé-Hoover, Langevin, and Bussi−Donadio−Parrinello (BDP).

fitting and extrapolation of the temperature data after the time average processing of the last 5 ns, which can ensure that the system has reached a steady state under nonequilibrium heat flux. According to Fourier's law, the interface thermal conductance (ITC) G can be defined as

$$G = \frac{J}{\Delta T} \tag{4}$$

It is worth noting that due to the existence of the fixed and the thermal bath area, the effective heat transfer area in the system is about 20 nm in length, as shown in Figure 1i. In addition, to avoid spurious effects related to the specific choice of the defect location, under the same defective concentration, three different samples were constructed by stochastically setting defects for semidefective Gr/h-BN in-plane heterostructures. For each sample, three sets of independent simulations with different initial velocities were performed. Finally, the statistical average of the nine results was taken as the final calculation result, which obviously can make it without loss of generality and more convincing.

RESULTS AND DISCUSSION

Method Validation with Pristine Gr/h-BN. First of all, the ITC values of pristine Gr/NB and Gr/BN were calculated by the NEMD method mentioned above to evaluate the feasibility of the simulation method. The Langevin thermostat

https://dx.doi.org/10.1021/acs.jpcc.0c10387
J. Phys. Chem. C 2021, 125, 2748−2760

applied the temperature of T_h = 330 K and T_c = 270 K respectively to the heat source and heat sink in the equilibrated system to generate a nonequilibrium heat flux from the Gr domain to the h-BN domain. In Figure 2a, it exemplarily shows the temperature profile of the Gr/NB along the heat flux direction after the system reaches the nonequilibrium steady state. Clearly, a discontinuous distribution of temperature is triggered at the interface, and a significant temperature jump is observed, indicating the existence of the Kapitza thermal resistance between Gr and h-BN. Further, the amplitude of the temperature jump ΔT is determined indirectly by linearly fitting and extrapolating the temperature profiles in the two components of the heterostructure. In addition, in order to maintain the nonequilibrium steady-state heat flux throughout the simulation process, the energy will be transferred almost equally from the heat source to the heat sink at the same time, as shown in Figure 2b. It is important to note here that on the nanoscale region, the interior and interface are tightly correlated, which gives rise to a complicated transport character. When the simulated size is smaller than the phonon mean free path (MFP), ITC will show obvious length dependence since the increase of the size will stimulate more long-wave phonons to participate in the transport. The semidefective heterostructure in this study will have a significantly lower MFP due to the presence of defects, and the phonon transport will mostly be in the diffusive transport state, which will undoubtedly reduce the dependence of ITC on length. In addition, since the main concern of this study is the effect of topological defects of the heterogeneous component on the ITC at the heterogeneous interface, the same size of 22.5 nm × 5 nm was used for all simulated samples.

It can be further calculated by eq 4 that at the temperature configuration of T_0 = 300 K, Δ = 0.1, the ITC values of Gr/NB and Gr/BN with the size of 22.5 nm × 5 nm are 15.57 ± 0.07 GW m^{-2} K^{-1} and 12.94 ± 0.14 GW m^{-2} K^{-1} respectively, which are within a reasonable range of results obtained by other studies.[20,32−37] As shown in Figure 3, under similar models and temperature conditions, the results obtained in this paper are in good agreement with those of existing studies using the Langevin thermostat. However, the ITC results of these studies are mainly distributed between 4 and 16 GW m^{-2} K^{-1} and have wide variability, which seems to depend on the difference in the choice of thermostat for achieving nonequilibrium heat flux in the NEMD method. The Nosé-Hoover (chain) thermostat[52,53] rescales the speed of all atoms and can only ensure that the average temperature of the constant temperature zone is the target temperature, which leads to the inaccuracy of temperature control. The Bussi−Donadio−Parrinello (BDP) thermostat[54] is developed on the basis of the Berendsen thermostat and has truly realized the temperature control method of the NVT ensemble. When using these two global thermostats, although local thermal equilibrium can also be satisfied, their local temperature control in the thermostated zone is not precise enough, which will affect the temperature distribution in the nonequilibrium heat transfer zone. Specifically, it results in a large effective temperature difference between the heat source and the heat sink,[55] and furthermore the temperature difference at the interface is also obtained to be large, which is exactly the fundamental reason for the underestimation of the ITC. Notably, the Langevin thermostat, with its locality and randomness, can reliably control the local temperature, so its performance is the best for NEMD simulation.[51,55,56] To this end, the simulations in this study all used Langevin local thermostat to set the heat source and heat sink. It is not difficult to find that under the same thermostat, the results of our study are basically consistent with the results of previous studies.[20,35] This means that the simulation process of this study has good feasibility, and it also guarantees the reliability of subsequent simulation results to a certain extent.

Effect of Defective Concentration on ITC and TR Factor. *Effect on ITC.* For the above four basic models, the influence of defective concentration on ITC was studied under the condition of T_0 = 300 K, Δ = 0.1; see Figure 4 for details.

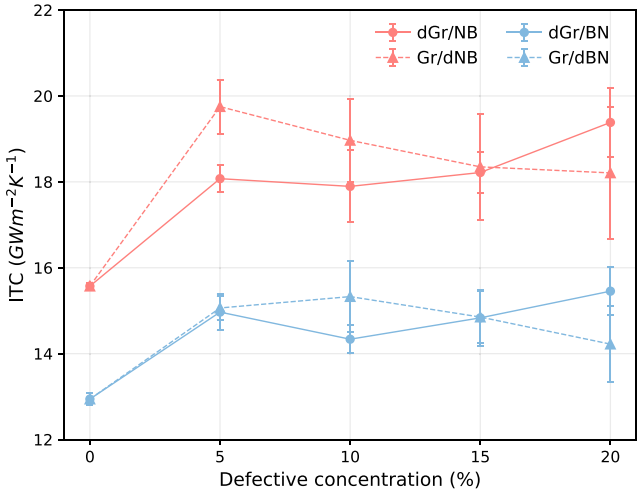

Figure 4. In the case of T_0 = 300 K, Δ = 0.1, the relationship between the ITC and the defective concentration of four different heterostructures, dGr/NB, Gr/dNB, dGr/BN, and Gr/dBN with a size of 22.5 nm × 5 nm. It includes five situations where the defective concentration is 0%, 5%, 10%, 15%, and 20%. The error bar for each data point is calculated from the standard deviation of the corresponding nine simulation results. The data of C−N group and C−B group are marked by red and blue respectively; the data of dGr group and dBN group are marked by circular and triangular data points, respectively. (See the text for a detailed explanation of grouping.)

Henceforth, for the calculation of ITC, this study only representatively considers the case where the heat source and heat sink are located in Gr and h-BN respectively; that is, the heat flux direction is from the Gr domain to the h-BN domain. For the four different heterostructures of dGr/NB, Gr/dNB, dGr/BN, and Gr/dBN, the following two perspectives will be used for comparative research, which will make the analysis of the results clearer and more organized. First, the four heterostructures were divided into the C−N group (including dGr/NB and Gr/dNB) and C−B group (including dGr/BN and Gr/dBN) based on the difference in atomic bonding configurations at the interface. In addition, due to the difference of defective object, they could be divided into the dGr group (including dGr/NB and dGr/BN) and the dBN group (including Gr/dNB and Gr/dBN).

Initially, we performed longitudinal analysis of the data shown in Figure 4, that is, a comparative analysis of the results of the C−N group and the C−B group. Indeed, the bonding configuration has a significant impact on the ITC of the heterostructures. Overall, for the same defective concentration, the ITC of a heterostructure with C−N bonding interface is

https://dx.doi.org/10.1021/acs.jpcc.0c10387
J. Phys. Chem. C 2021, 125, 2748−2760

about 20% higher than that with C−B bonding interface. To the best of our knowledge, C−N and C−B are two bonding methods that belong to the category of covalent bonds, but the former has obvious advantages in strength.[33] The higher-strength bonding configuration reduces the adverse effect of the heterogeneity of the materials on both sides of the interface on the phonon transmission to a certain extent, which gives the heterostructures with the C−N interface certain advantages in heat transfer. As proof, the related research in Figure 3 has also shown similar results as ours.[32,33,37]

Afterward, the data shown in Figure 4 will be analyzed laterally, that is, the relationship between the ITC of the semidefective heterostructures and the defective concentration. On the whole, whether it is the C−N group or the C−B group semidefectiveness has a significant improvement on ITC. It means that without changing the original interface, through the topological design of the base material, the ITC of the Gr/h-BN can be effectively improved. Notably, through further analysis, it was found that the ITC of the semidefective heterostructures with the change of the defective concentration mainly shows a completely different trend due to the difference of the defective base material. For the dGr group, the ITC basically maintains an increasing trend with the increase of the defective concentration. In contrast, the results of the dBN group show that the ITC has a trend of rising first and then falling with the increase of the defective concentration. From a local point of view, when the defective concentration is over 10%, the ITC of the dGr group steadily rises with the increase of the defective concentration, while the dBN group is just the opposite. Comparing the two components of the heterostructures, it is not difficult to find that the thermal conductivity of pristine Gr (~2460 W m^{-1} K^{-1}) is about 3.75 times that of pristine h-BN (~656 W m^{-1} K^{-1}).[57,58] In the dGr group, the defectiveness of Gr greatly reduces its thermal conductivity, but at the same time it makes this property closer to the h-BN on the other side of the interface. On the contrary, after defectiveness of h-BN, the gap between it and Gr becomes more and more significant, which highlights the heterogeneity of phonon transmission of the components on both sides of the interface.

In addition, it is worth noting that for the heterostructures of the dBN group with an defective concentration over 20%, the entire heterostructure may collapse due to the instability of the defective component, while it does not exist in the dGr group. Furthermore, as shown in Table 1, with the continuous increase of the defective concentration, the ITC of the dGr group showed a steady increase. And at a higher defective concentration (about 30%), its ITC can be up to about 50% greater than that of the pristine Gr/NB. Therefore, in comparison, the dGr/NB heterostructure is undoubtedly a better choice in terms of improving ITC.

Table 1. ITC of dGr/NB and dGr/BN Heterostructures Varies with Defective Concentration ([a])

	ITC (GW m^{-2} K^{-1})	
defective concentration (%)	dGr/NB	dGr/BN
0	15.57 ± 0.07	12.94 ± 0.14
5	18.07 ± 0.32	14.97 ± 0.42
10	17.89 ± 0.84	14.34 ± 0.33
15	18.22 ± 0.48	14.83 ± 0.65
20	19.38 ± 0.81	15.45 ± 0.56
25	21.21 ± 1.04	16.63 ± 0.39
30	23.57 ± 1.77	17.75 ± 1.48
40	23.84 ± 1.96	18.00 ± 1.31

[a]The errors are all calculated from the standard deviation of nine independent simulations.

Furthermore, the above results will be analyzed in detail through in-depth understanding of phonon activity. Phonon density of state (PDOS), a classic method to characterize phonon activity in materials, is usually used to understand the behavior of heat transfer at the interface.[35−37] Since the energy of phonons is essentially the energy of atomic vibration, the PDOS in the frequency domain can be obtained by performing the following Fourier transformation on the velocity autocorrelation function of atoms:

$$\mathrm{PDOS}_\alpha(\omega) = \int_{-\infty}^{+\infty} \langle v_\alpha(t) v_\alpha(0)\rangle e^{-2\pi i\omega t}\, \mathrm{d}t \quad (\alpha = x, y, z) \tag{5}$$

where ω is the vibration frequency, $\langle v_\alpha(t) v_\alpha(0)\rangle$ is the autocorrelation function of the velocity of the atom in the direction α at relevant time t. When $\alpha = x, y, z$, eq 5 corresponds to the in-plane transverse acoustic mode (TA), in-plane longitudinal acoustic mode (LA), and out-of-plane acoustic mode (ZA), respectively. For the polarized PDOS in this study, the average value of TA and LA is regarded as the overall in-plane PDOS, and only in-plane and out-of-plane phonons are distinguished. Notably, from the perspective of lattice dynamics, the key factor that determines the transmission of phonons between two heterogeneous materials is the overlap of PDOS between them. In order to quantify the overlap of PDOS between components in a heterogeneous system, the overlap factor S is introduced:

$$S = \frac{\int_0^\infty P_A(\omega) P_B(\omega)\, \mathrm{d}\omega}{\int_0^\infty P_A(\omega)\, \mathrm{d}\omega \times \int_0^\infty P_B(\omega)\, \mathrm{d}\omega} \tag{6}$$

where $P_A(\omega)$ and $P_B(\omega)$ represent the PDOS of heterogeneous components A and B at frequency ω. Additionally, the overlap factors of in-plane and out-of-plane PDOS are denoted by S_{in} and S_{out} respectively.

According to eqs 5−6, three independent calculations were performed for each set of models by the different stochastic initial velocity, and the PDOS and the PDOS overlap factor S, which reflect the phonon coupling status, were obtained through statistical average. As shown in Figure 5a−c, the PDOS calculation results of the two components in the dGr/NB heterostructures with an defective concentration of 0%, 10%, and 20% are exemplarily plotted. It is not difficult to find that with the increase of the defective concentration, the PDOS of the defective domain will vary significantly, which is mainly reflected in the substantial weakening of in-plane high-frequency PDOS and the improvement of out-of-plane low-frequency PDOS. In order to quantify this change, the S_{in} and S_{out} of the four semidefective heterostructures at different defective concentrations was further calculated by eq 6; see Figure 5d−e for details. As the defective concentration increases, the S_{out} of the two components in the four heterostructures all rises monotonically with different magnitudes, while the S_{in} shows a downward trend, which confirms the intuitive observation results in Figure 5a−c. Notably, it has been proved that the in-plane part of phonon activity plays a far less role in heat transfer or phonon coupling than the out-of-plane part;[37,59] that is to say, the out-of-plane

https://dx.doi.org/10.1021/acs.jpcc.0c10387
J. Phys. Chem. C 2021, 125, 2748−2760

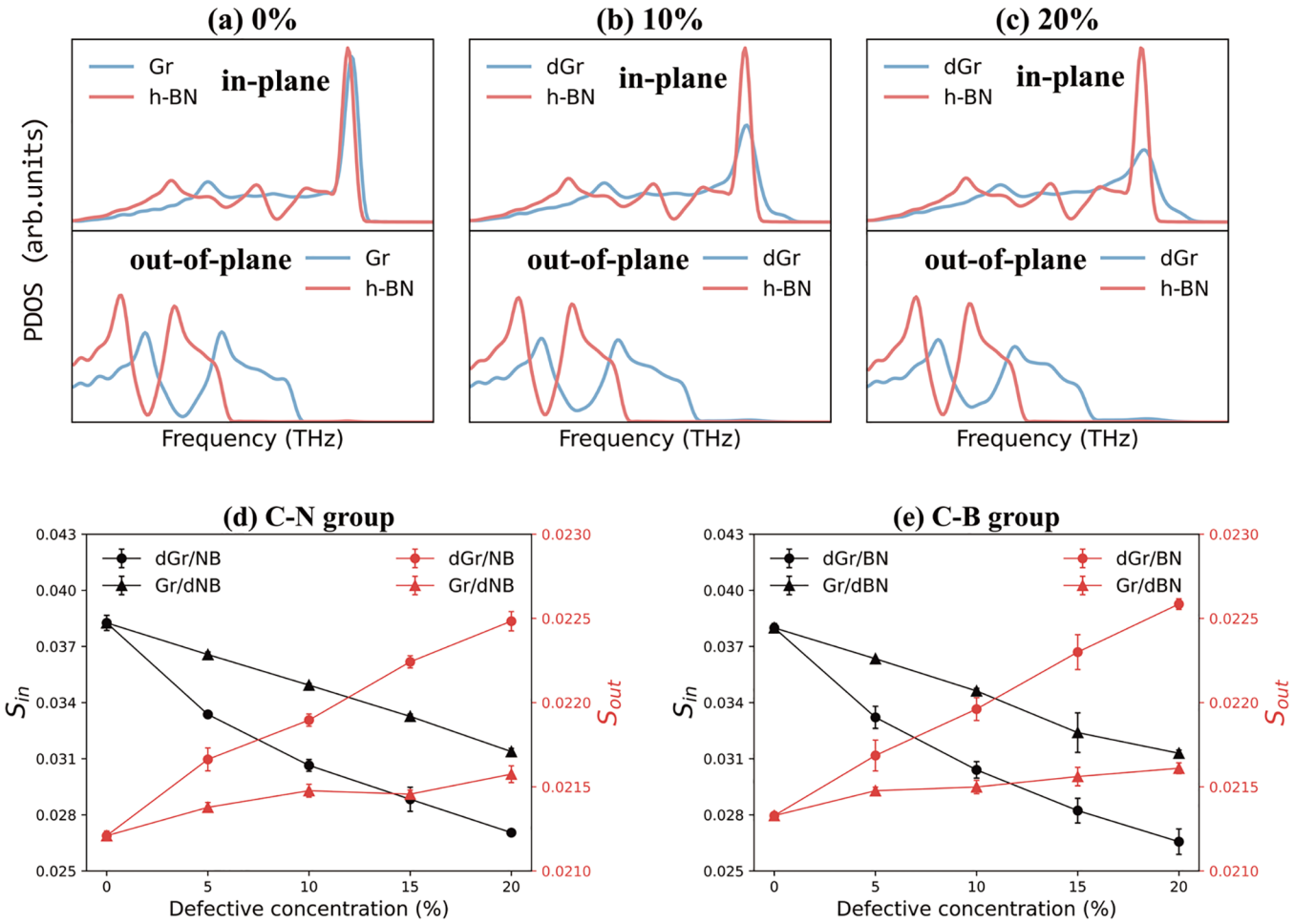

Figure 5. (a−c) Schematic diagrams of in-plane and out-of-plane PDOS of Gr domain and h-BN domain in dGr/NB heterostructures with defective concentrations of 0%, 10%, and 20%, respectively. (d−e) In the C−N group and C−B group, the PDOS overlap factor of in-plane (S_{in}) and out-of-plane (S_{out}) varies with the defective concentration in different heterostructures. The error bar is represented by the standard deviation of the corresponding nine simulation statistical averages. (Each model of defective concentration included three sets of stochastic defectiveness models, and each set of defectiveness models were performs three independent calculations with different initial velocities.)

phonon activity has a decisive effect on heat transfer. As a result, the improvement of ITC by defectiveness in this study can be well explained from this perspective. However, regardless of whether it is the C−N group or the C−B group, even though increases with the increase of defective concentration, the dGr group and the dBN group still show great differences. Specifically, as the defective concentration increases, the improvement rate of in the dGr group is much higher than that in the dBN group, which means that the improvement of the ITC in the dGr group will be more substantial and stable.

In more depth, for the significant difference between the dGr group and dBN group in the ITC affected by the defective concentration, further exploration was carried out through phonon localization effect. The difference between the dGr group and the dBN group mainly lies in the different objects of defectiveness, and atomic defects and heterogeneous interfaces are the critical factors that trigger the phonon localization effect, which is a common phenomenon in heat transfer. For the study of phonon localization effect, calculating the phonon participation rate (PPR) is an effective avenue, which can implicitly include all orders of anharmonic scattering through MD simulation:[60]

$$\mathrm{PPR}(\omega) = \frac{1}{N}\frac{\left(\sum_i \mathrm{PDOS}_i^2(\omega)\right)^2}{\sum_i \mathrm{PDOS}_i^4(\omega)} \tag{7}$$

where $\mathrm{PDOS}_i(\omega)$ is the local PDOS of atom numbered i calculated by eq 5, and N is the total number of atoms involved in the calculation. PPR can be considered as the fraction of atoms participating in a certain mode ω, which can effectively indicate whether a specific mode has localized characteristics. In order to further operationalize the concept of phonon localization, we defined the localization state as a state where the PPR is less than 0.4.

For each group of models to be studied, by calculating the PDOS of each atom in the heat transfer zone, the PPR of the corresponding heterostructure was further calculated, which includes the process of statistical averaging through three independent simulations with the different stochastic initial velocity. In Figure 6, the PPR calculation results of the four semidefective heterostructures in this study are exemplarily plotted at the defective concentration of 0%, 10%, and 20%. Before the introduction of topological defects; that is, when the defective concentration is 0%, almost all phonons in the whole frequency range are in the delocalized mode, namely, PPR > 0.4. However, after semidefectiveness, the PPR results of the

https://dx.doi.org/10.1021/acs.jpcc.0c10387
J. Phys. Chem. C 2021, 125, 2748−2760

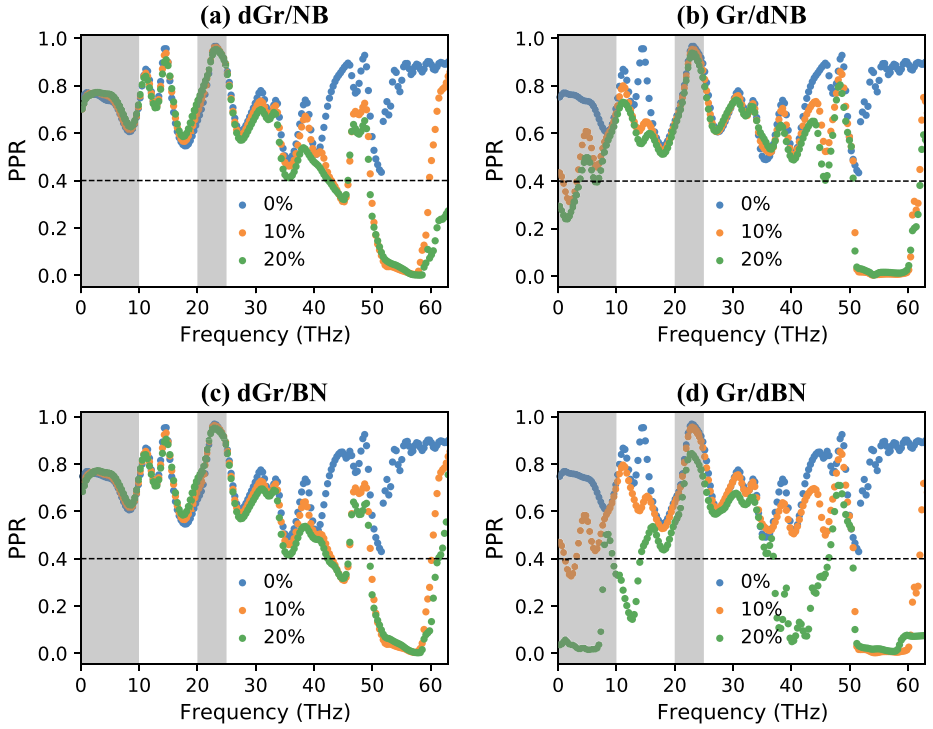

Figure 6. Calculation results of the phonon participation rate of the four semidefective heterostructures (a) dGr/NB, (b) Gr/dNB, (c) dGr/BN, and (d) Gr/dBN with defective concentrations of 0%, 10%, and 20%, respectively. The black horizontal dashed line is the reference line with PPR = 0.4, which can be used to effectively define whether the phonons of a specific mode have localized characteristics. The gray vertical shade part covers the low-frequency phonon range (0−10 THz and 20−25 THz), which plays a decisive role in heat transfer.

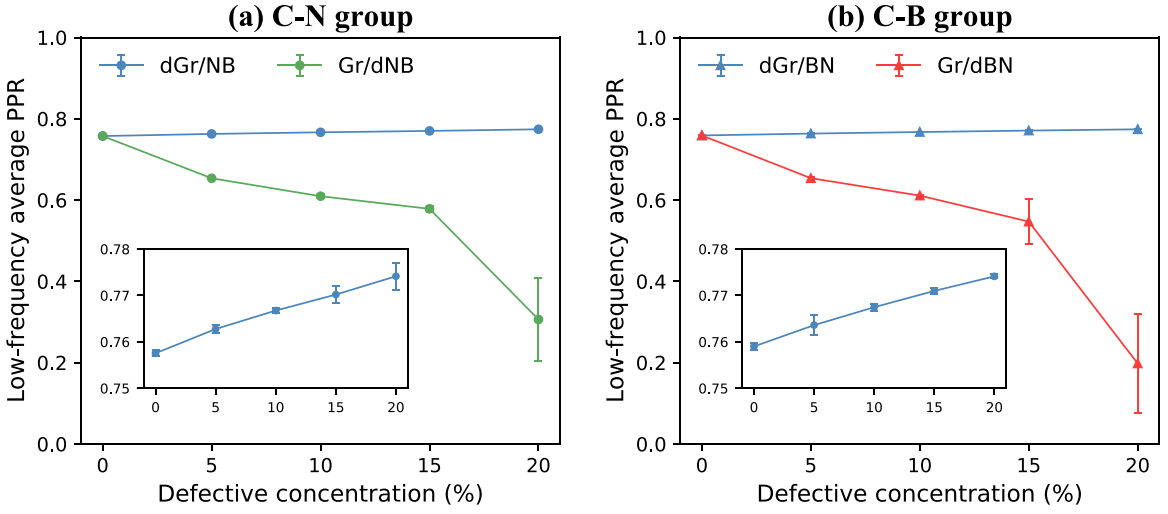

Figure 7. Relationship between the low-frequency average phonon participation rate with defective concentration in (a) C−N group and (b) C−B group heterostructures. The low-frequency band contains sections with frequencies of 0−10 THz and 20−25 THz. The data of the dGr group are shown enlarged by the detail map, which gives a clearer picture of the trend of their values.

four semidefective heterostructures show completely different variations. For the heterostructures of the dGr group in Figure 6a,c, as the defective concentration increases, the amplitude of PPR in the high-frequency part of greater than 30 THz, especially 50−60 THz, sharply decreases and shows a local mode characteristic. Surprisingly, the PPR results of the low-frequency part are slightly improved. In contrast, the results of the dBN group in Figure 6b,d show that the weakening effect of semidefectiveness on PPR is comprehensive and covers the entire frequency domain.

Owing to acoustic mode phonons (low-frequency bands) have higher group velocities than optical mode phonons (high-frequency bands), their heat carrier efficiency is higher, and they make up most of the contribution to heat transfer. Therefore, in Figure 7, the variation of the low-frequency average PPR of the four semidefective heterostructures with the defective concentration was counted, which includes the parts with frequencies of 0−10 THz and 20−25 THz. It is obvious that the low-frequency average PPR of the heterostructures in the dGr group increases slightly but steadily as a function of the defective concentration. On the

https://dx.doi.org/10.1021/acs.jpcc.0c10387
J. Phys. Chem. C 2021, 125, 2748−2760

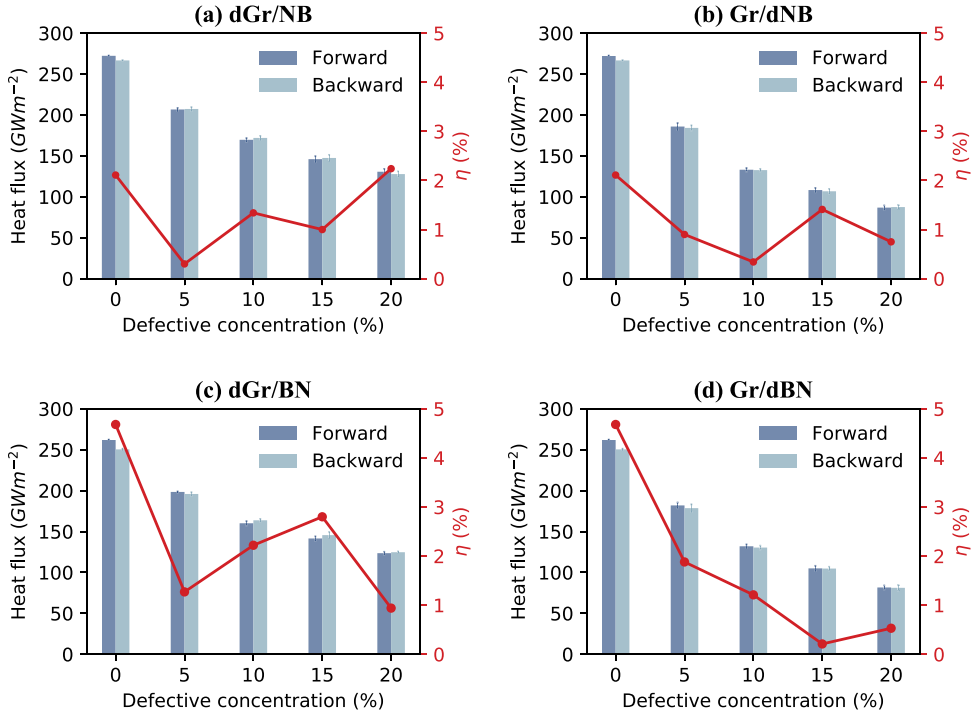

Figure 8. (a–d) Under the condition of T_0 = 300 K, |Δ| = 0.1, the magnitude of the forward heat flux (from the Gr domain to the h-BN domain), the magnitude of the reverse heat flux (from the h-BN domain to the Gr domain) and the TR factor in the four semidefective Gr/h-BN heterostructures as a function of defective concentration. The error bar of the heat flux is represented by the standard deviation of the nine simulation results, and their average result is used to calculate the TR factor.

contrary, the corresponding low-frequency average PPR of the dBN group dropped monotonically and significantly. It shows that after the h-BN domain undergoes a higher concentration of defects, the atomic vibration of the entire system is greatly affected. In particular, the low-frequency phonons, which have a major contribution to heat transfer, decrease sharply, which reduces the thermal conductivity of the base material, causes localization of the phonons, and hinders the phonon transmission across the interface. This explains well the phenomenon that with the increase of the defective concentration, the ITC of the dGr group steadily increases, while the ITC of the dBN group shows a downward trend.

Through the comparison of interface bonding configuration, the exploration of PDOS overlap factor and phonon localization effect, the underlying mechanism of the ITC of semidefective Gr/h-BN heterostructures with the change of defective concentration is obtained. Initially, the interface bonding configuration is used as the classification standard. Since the high-strength interface bonding is more conducive to phonon transmission, the ITC of the C–N group heterostructures with a higher interface bonding strength is significantly higher than that of the C–B group as a whole. Furthermore, for different defective objects, the trend of the ITC with the defective concentration depends on the combined influence of phonon coupling on both sides of the interface (determined by the PDOS overlap factor) and the phonon localization effect of the heterostructure (determined by the low-frequency average PPR). The strengthen of phonon coupling on both sides of the interface determines the overall improvement of its ITC. However, with the increase of the defective concentration, the increasingly prominent low-frequency phonon localization effect caused the ITC of the dBN group to show a downward trend, while the increase of the low-frequency PPR of the dGr group caused its ITC to continue to rise steadily. This provides inspiration for improving the ITC of Gr/h-BN in-plane heterostructures through defect engineering as a thermal device.

Effect on TR Factor. The thermal rectification (TR) effect, an important physical phenomenon, means that heat can be easily transferred in one direction of the structure, but it is much more difficult in the opposite direction. In recent years, the research on the TR effect based on the Gr/h-BN in-plane heterostructures has received extensive attention,[12,36] which is a revelation for the development and application of thermal logic devices. Next, a series of simulations were performed to determine whether there is a clear TR effect in the semidefective heterostructures of our study. On the basis of the previously described models, the reverse heat flux was realized by swapping the heat source and the heat sink, and their value were recorded, thereby the TR factor was calculated by

$$\eta = \frac{|J_{\text{Forward}} - J_{\text{Backward}}|}{J_{\text{Backward}}} \times 100\% \tag{8}$$

where the heat flux from the Gr domain to the h-BN domain is defined as J_{Forward}; that is, Δ > 0. Conversely, when Δ < 0, J_{Backward} represents the heat flux from h-BN domain to the Gr domain.

Under T_0 = 300 K, the heat flux was calculated when Δ = ±0.1 separately, and the TR factor was also obtained by eq 8, as shown in Figure 8. Initially, in terms of the trend of heat flux with defective concentration, the four semidefective heterostructures show little difference. With the gradual increase of the defective concentration, the heat flux of the heterostructure shows a steady downward trend, and it can be reduced to less than half of the pristine sample at 20% defective concentration.

https://dx.doi.org/10.1021/acs.jpcc.0c10387
J. Phys. Chem. C 2021, 125, 2748–2760

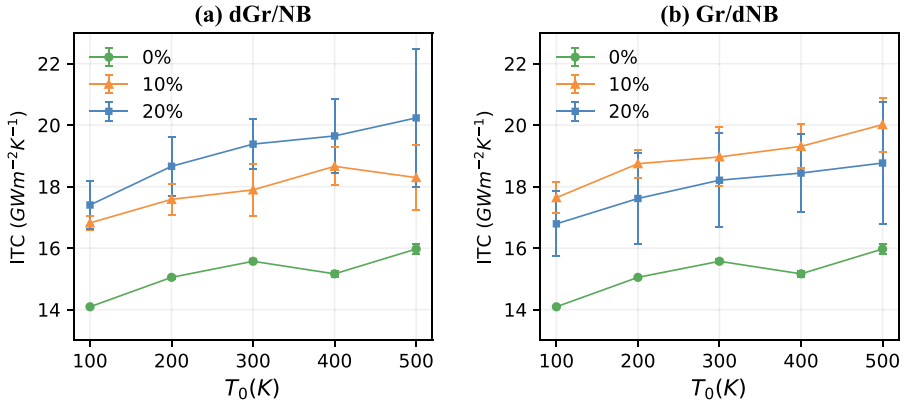

Figure 9. ITC of (a) Gr/NB and (b) Gr/dNB heterostructures at the defective concentration of 0%, 10%, and 20% varies with the average temperature. The normalized temperature difference between the heat source and heat sink of all simulation systems is set to 0.1. (Error bars are represented by the standard deviation of nine independent simulations.)

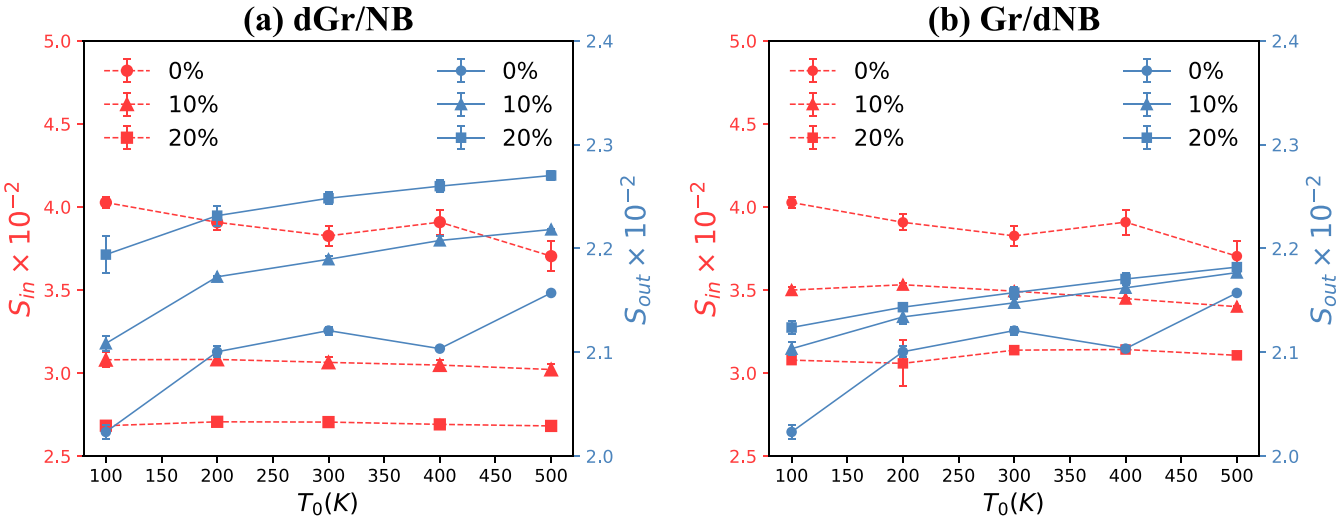

Figure 10. Variation of the in-plane and out-of-plane phonon overlap factors with an average temperature T_0 on both sides of the interface for (a) dGr/NB and (b) Gr/dNB heterostructures with defective concentrations of 0%, 10%, and 20%. (Error bars are represented by the standard deviation of nine independent simulations.)

This means that defectiveness has a significant weakening effect on the overall heat transfer ability of the heterostructures, which is consistent with our common notion. Notably, the difference between the magnitude of the heat flux in the opposite direction produced by swapping the temperature bias of the system is very slight, which is reflected in the TR factor of about 2% in all cases, and the maximum value does not exceed 5%. For such a small and almost negligible TR factor, it may be derived from random deviations among independent simulations, and it cannot effectively prove the existence of the TR effect in the system. In addition, the Langevin local thermostat used to generate heat flux in this study effectively avoids the artifacts of unphysical TR that may be caused by the Nosé-Hoover thermostat, which ensures the reliability of the above results.[55] Thus, there is no obvious TR effect in the semidefective Gr/h-BN in-plane heterostructures in this study.

Effect of Temperature on ITC. As a potential thermal device material, its working environment is bound to include a wide range of temperature conditions. Therefore, temperature, a physical quantity closely related to heat, is often an object that cannot be ignored in the research involving micro-nanoscale heat transfer. According to the temperature configuration of the simulation system in this study (see the section "MD simulation details" for details), the temperature specifically includes the following two effects: average temperature (T_0), normalized temperature difference between heat source and heat sink (Δ). On the basis of the above results, it is not difficult to find that the difference in the atomic bonding configuration of the interface only has an effect on the amplitude of the ITC, but not on the trend with defective concentration. Meanwhile, on the basis of the fundamental principle of improving the ITC of heterostructures, the C−N group heterostructures will be selected in this section. Further, the C−N group heterostructures with defective concentrations of 0%, 10%, and 20% will be used as representative for calculation and analysis.

Effect of Average Temperature (T_0). In this section, the ITC values of two semidefective heterostructures of the C−N group with an defective concentration of 0%, 10%, and 20% were calculated at 100−500 K with an interval of 100 K and plotted in Figure 9, where Δ = 0.1. Each of the heterostructures has been simulated nine times independently, which effectively avoids the influence of the specificity of the structure defectiveness and the randomness of the simulation initial velocity seed on the calculation results. On the whole,

https://dx.doi.org/10.1021/acs.jpcc.0c10387
J. Phys. Chem. C 2021, 125, 2748−2760

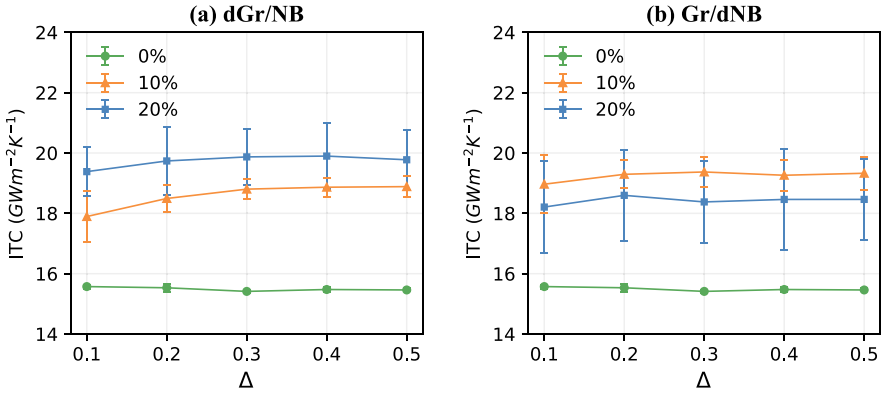

Figure 11. At an average temperature of 300 K, the ITC of (a) dGr/NB and (b) Gr/dNB heterostructures with defective concentrations of 0%, 10%, and 20% varies with the normalized temperature difference between the heat source and the heat sink. (Error bars are represented by the standard deviation of nine independent simulations.)

ITC for each group of heterostructures is expected to monotonically rise as a function of T_0. In other words, ITC and T_0 basically have a positive correlation, which is caused by the enhancement of the anharmonicity of atomic interactions brought about by a higher temperature. The increase in temperature intensifies the vibration of atoms, and at the same time strengthens the transmission efficiency of phonons through inelastic scattering, which is then manifested as an increase in the ITC value. It is worth noting that the error bar range of the ITC for the semidefective heterostructures with high defective concentration is wider, which is especially obvious at higher temperatures. For semidefective heterostructures, the introduction of defects inevitably leads to structural instability to a certain extent, and this instability is more prominent with the intensification of atomic vibrations due to high temperature. Nevertheless, whether it is semidefective or increasing the temperature of system, there is a visible increase in its ITC, which has a guiding significance for the development and application of thermal devices.

Additionally, in order to provide a more convincing explanation of how the ITC varies with temperature in Figure 9, the in-plane and out-of-plane phonon overlap factors between the components of the above-mentioned heterostructures were calculated, as Figure 10 shows. In general, as the temperature rises, the S_{in} of all models involved in the calculation remains almost unchanged or slightly decreases. However, the S_{out}, which occupies an absolute proportion in the contribution of heat transfer or phonon coupling, shows a clear upward trend. The degree of overlap of the out-of-plane PDOS (S_{out}) indicated by the red data in Figure 10 has good consistency with the ITC in Figure 9, which further shows that the heat transfer capacity across the interface mainly depends on the coupling of phonons on both sides of the interface.

Effect of Temperature Difference. In Figure 11, it shows the relationship between the ITC and the Δ of the two semidefective heterostructures in the C−N group with an defective concentration of 0%, 10%, and 20% at an average temperature of 300 K. It is not difficult to find that under the condition of a constant average temperature, the influence of the normalized temperature difference Δ on the ITC can be negligible. ITC, as a physical property that characterizes the heat transfer capacity across the heterogeneous interface, is closely related to the state of the system, such as the above-mentioned structural configuration and the average temperature. However, the normalized temperature difference can be regarded as the process of reaching the average temperature, so it will not have a significant impact on ITC. In general, this means that the ITC of the semidefective heterostructures in this study is related to the average temperature of the system rather than the normalized temperature difference, which further broadens the scope of its application conditions to a certain extent.

CONCLUSION

In summary, a class of semidefective Gr/h-BN in-plane heterostructures has been designed based on defect engineering, and the heat transfer across the interface has also been systematically studied from two aspects of defective configuration and temperature through the NEMD method. Unexpectedly, the defectiveness of a certain component in the heterostructure, which seems to reduce the efficiency of phonon transmission, can improve the ITC without changing the interfacial structure. The heterostructure with the C−N bond configuration at the interface relies on the obvious advantages in the heat transfer of phonons caused by the higher covalent bond strength, making its ITC significantly higher than the heterostructures with the C−B bond. Notably, while the ITC of the heterostructures has been improved overall, it also shows different trends as the defective concentration increases due to the different defective objects. Through the joint analysis of the PDOS overlap and phonon participation rate, it is found that on the basis of strengthening the phonon coupling across the interface, the defectiveness of Gr further increases the low-frequency PPR of the heterostructures, while the defectiveness of h-BN makes the low-frequency phonons appear obvious localization effect. In addition, the influence of temperature on the ITC is also discussed. These findings provide a new insight for improving the ITC in the 2D in-plane heterostructures, which may extend the application of defect engineering in the thermal management and thermal design of nanomaterials.

AUTHOR INFORMATION

Corresponding Author

Qiang Han − *Department of Engineering Mechanics, School of Civil Engineering and Transportation, South China University of Technology, Guangzhou, Guangdong Province 510640, People's Republic of China;* orcid.org/0000-0002-9972-461X; Email: emqhan@scut.edu.cn

https://dx.doi.org/10.1021/acs.jpcc.0c10387
J. Phys. Chem. C 2021, 125, 2748−2760

Author

Xin Wu − *Department of Engineering Mechanics, School of Civil Engineering and Transportation, South China University of Technology, Guangzhou, Guangdong Province 510640, People's Republic of China*

Complete contact information is available at: https://pubs.acs.org/10.1021/acs.jpcc.0c10387

Notes

The authors declare no competing financial interest.

■ ACKNOWLEDGMENTS

The authors are grateful for support from the National Natural Science Foundation of China (11972160), Guangdong Basic and Applied Basic Research Foundation (2019A1515011900), Science and Technology Program of Guangzhou, China (202002030367).

■ REFERENCES

(1) Novoselov, K. S.; Geim, A. K.; Morozov, S. V.; Jiang, D.; Zhang, Y.; Dubonos, S. V.; Grigorieva, I. V.; Firsov, A. A. Electric Field Effect in Atomically Thin Carbon Films. *Science* **2004**, *306*, 666−669.

(2) Wang, L.; Wu, B.; Chen, J.; Liu, H.; Hu, P.; Liu, Y. Monolayer hexagonal boron nitride films with large domain size and clean interface for enhancing the mobility of graphene-based field-effect transistors. *Adv. Mater.* **2014**, *26*, 1559−1564.

(3) Yi, F.; Ren, H.; Shan, J.; Sun, X.; Wei, D.; Liu, Z. Wearable energy sources based on 2D materials. *Chem. Soc. Rev.* **2018**, *47*, 3152−3188.

(4) He, L.; Guo, S.; Lei, J.; Sha, Z.; Liu, Z. The effect of Stone−Thrower−Wales defects on mechanical properties of graphene sheets − A molecular dynamics study. *Carbon* **2014**, *75*, 124−132.

(5) Levendorf, M. P.; Kim, C.-J.; Brown, L.; Huang, P. Y.; Havener, R. W.; Muller, D. A.; Park, J. Graphene and boron nitride lateral heterostructures for atomically thin circuitry. *Nature* **2012**, *488*, 627−632.

(6) Novoselov, K. S.; Mishchenko, A.; Carvalho, A.; Neto, A. H. C. 2D materials and van der Waals heterostructures. *Science* **2016**, *353*, aac9439.

(7) Eshkalak, K. E.; Sadeghzadeh, S.; Jalaly, M. Mechanical properties of defective hybrid graphene-boron nitride nanosheets: A molecular dynamics study. *Comput. Mater. Sci.* **2018**, *149*, 170−181.

(8) Li, B.; Wang, L.; Casati, G. Thermal diode: rectification of heat flux. *Phys. Rev. Lett.* **2004**, *93*, 184301.

(9) Casati, G. Controlling the heat flow: now it is possible. *Chaos* **2005**, *15*, 015120.

(10) Chang, C. W.; Okawa, D.; Majumdar, A.; Zettl, A. Solid-State Thermal Rectifier. *Science* **2006**, *314*, 1121−1124.

(11) Pal, S.; Puri, I. K. Thermal AND Gate Using a Monolayer Graphene Nanoribbon. *Small* **2015**, *11*, 2910−2917.

(12) Chen, X.-K.; Xie, Z.-X.; Zhou, W.-X.; Tang, L.-M.; Chen, K.-Q. Thermal rectification and negative differential thermal resistance behaviors in graphene/hexagonal boron nitride heterojunction. *Carbon* **2016**, *100*, 492−500.

(13) Wang, Y.; Vallabhaneni, A.; Hu, J.; Qiu, B.; Chen, Y. P.; Ruan, X. Phonon lateral confinement enables thermal rectification in asymmetric single-material nanostructures. *Nano Lett.* **2014**, *14*, 592−596.

(14) Zhang, H.; Fonseca, A. F.; Cho, K. Tailoring Thermal Transport Property of Graphene through Oxygen Functionalization. *J. Phys. Chem. C* **2014**, *118*, 1436−1442.

(15) Nobakht, A. Y.; Gandomi, Y. A.; Wang, J.; Bowman, M. H.; Marable, D. C.; Garrison, B. E.; Kim, D.; Shin, S. Thermal rectification via asymmetric structural defects in graphene. *Carbon* **2018**, *132*, 565−572.

(16) Yousefi, F.; Khoeini, F.; Rajabpour, A. Thermal conductivity and thermal rectification of nanoporous graphene: A molecular dynamics simulation. *Int. J. Heat Mass Transfer* **2020**, *146*, 118884.

(17) Wei, N.; Li, S.; Zhang, Y.; Chen, J.; Chen, Y.; Zhao, J. Thermal rectification of graphene on substrates with inhomogeneous stiffness. *Carbon* **2019**, *154*, 81−89.

(18) Wei, A.; Lahkar, S.; Li, X.; Li, S.; Ye, H. Multilayer Graphene-Based Thermal Rectifier with Interlayer Gradient Functionalization. *ACS Appl. Mater. Interfaces* **2019**, *11*, 45180−45188.

(19) Chen, X.-K.; Pang, M.; Chen, T.; Du, D.; Chen, K.-Q. Thermal Rectification in Asymmetric Graphene/Hexagonal Boron Nitride van der Waals Heterostructures. *ACS Appl. Mater. Interfaces* **2020**, *12*, 15517−15526.

(20) Li, T.; Tang, Z.; Huang, Z.; Yu, J. Substrate effects on the thermal performance of in-plane graphene/hexagonal boron nitride heterostructures. *Carbon* **2018**, *130*, 396−400.

(21) Liu, X.; Zhang, G.; Zhang, Y.-W. Graphene-based thermal modulators. *Nano Res.* **2015**, *8*, 2755−2762.

(22) Song, J.; Xu, Z.; He, X.; Cai, C.; Bai, Y.; Miao, L.; Wang, R. Effect of strain and defects on the thermal conductance of the graphene/hexagonal boron nitride interface. *Phys. Chem. Chem. Phys.* **2020**, *22*, 11537−11545.

(23) Zou, J.-H.; Xu, X.-T.; Cao, B.-Y. Size-dependent mode contributions to the thermal transport of suspended and supported graphene. *Appl. Phys. Lett.* **2019**, *115*, 123105.

(24) Cao, B.-Y.; Zou, J.-H.; Hu, G.-J.; Cao, G.-X. Enhanced thermal transport across multilayer graphene and water by interlayer functionalization. *Appl. Phys. Lett.* **2018**, *112*, 041603.

(25) Ci, L.; Song, L.; Jin, C.; Jariwala, D.; Wu, D.; Li, Y.; Srivastava, A.; Wang, Z. F.; Storr, K.; Balicas, L.; Liu, F.; Ajayan, P. M. Atomic layers of hybridized boron nitride and graphene domains. *Nat. Mater.* **2010**, *9*, 430−435.

(26) Liu, Z.; Ma, L.; Shi, G.; Zhou, W.; Gong, Y.; Lei, S.; Yang, X.; Zhang, J.; Yu, J.; Hackenberg, K. P.; Babakhani, A.; Idrobo, J.-C.; Vajtai, R.; Lou, J.; Ajayan, P. M. In-plane heterostructures of graphene and hexagonal boron nitride with controlled domain sizes. *Nat. Nanotechnol.* **2013**, *8*, 119−124.

(27) Han, G. H.; Rodriguez-Manzo, J. A.; Lee, C.-W.; Kybert, N. J.; Lerner, M. B.; Qi, Z. J.; Dattoli, E. N.; Rappe, A. M.; Drndic, M.; Johnson, A. T. C. Continuous Growth of Hexagonal Graphene and Boron Nitride In-Plane Heterostructures by Atmospheric Pressure Chemical Vapor Deposition. *ACS Nano* **2013**, *7*, 10129−10138.

(28) Liu, L.; Park, J.; Siegel, D. A.; McCarty, K. F.; Clark, K. W.; Deng, W.; Basile, L.; Idrobo, J. C.; Li, A.-P.; Gu, G. Heteroepitaxial Growth of Two-Dimensional Hexagonal Boron Nitride Templated by Graphene Edges. *Science* **2014**, *343*, 163−167.

(29) Kim, G.; Lim, H.; Ma, K. Y.; Jang, A.-R.; Ryu, G. H.; Jung, M.; Shin, H.-J.; Lee, Z.; Shin, H. S. Catalytic Conversion of Hexagonal Boron Nitride to Graphene for In-Plane Heterostructures. *Nano Lett.* **2015**, *15*, 4769−475.

(30) Chiu, M.-H.; Zhang, C.; Shiu, H.-W.; Chuu, C.-P.; Chen, C.-H.; Chang, C.-Y. S.; Chen, C.-H.; Chou, M.-Y.; Shih, C.-K.; Li, L.-J. Determination of band alignment in the single-layer MoS2/WSe2 heterojunction. *Nat. Commun.* **2015**, *6*, 7666.

(31) Shi, J.; Liu, M.; Wen, J.; Ren, X.; Zhou, X.; Ji, Q.; Ma, D.; Zhang, Y.; Jin, C.; Chen, H.; Deng, S.; Xu, N.; Liu, Z.; Zhang, Y. All Chemical Vapor Deposition Synthesis and Intrinsic Bandgap Observation of MoS2 /Graphene Heterostructures. *Adv. Mater.* **2015**, *27*, 7086−7092.

(32) Liu, F.; Zou, R.; Hu, N.; Ning, H.; Yan, C.; Liu, Y.; Wu, L.; Mo, F.; Fu, S. Enhancement of thermal energy transport across the graphene/h-BN heterostructure interface. *Nanoscale* **2019**, *11*, 4067−4072.

(33) Liu, X.; Zhang, G.; Zhang, Y.-W. Topological Defects at the Graphene/h-BN interface Abnormally Enhance Its Thermal Conductance. *Nano Lett.* **2016**, *16*, 4954−4959.

(34) Hong, Y.; Zhang, J.; Zeng, X. C. Thermal contact resistance across a linear heterojunction within a hybrid graphene/hexagonal boron nitride sheet. *Phys. Chem. Chem. Phys.* **2016**, *18*, 24164−24170.

(35) Li, M.; Zheng, B.; Duan, K.; Zhang, Y.; Huang, Z.; Zhou, H. Effect of Defects on the Thermal Transport across the Graphene/Hexagonal Boron Nitride Interface. *J. Phys. Chem. C* **2018**, *122*, 14945−14953.
(36) Zhang, Y.; Pei, Q.-X.; Wang, C.-M.; Yang, C.; Zhang, Y.-W. Interfacial Thermal Conductance and Thermal Rectification of Hexagonal BCnN/Graphene In-Plane Heterojunctions. *J. Phys. Chem. C* **2018**, *122*, 22783−22789.
(37) Liang, T.; Zhou, M.; Zhang, P.; Yuan, P.; Yang, D. Multilayer in-plane graphene/hexagonal boron nitride heterostructures: Insights into the interfacial thermal transport properties. *Int. J. Heat Mass Transfer* **2020**, *151*, 119395.
(38) Gao, Y.; Zhang, Y.; Chen, P.; Li, Y.; Liu, M.; Gao, T.; Ma, D.; Chen, Y.; Cheng, Z.; Qiu, X.; Duan, W.; Liu, Z. Toward single-layer uniform hexagonal boron nitride-graphene patchworks with zigzag linking edges. *Nano Lett.* **2013**, *13*, 3439−3443.
(39) Liu, M.; Li, Y.; Chen, P.; Sun, J.; Ma, D.; Li, Q.; Gao, T.; Gao, Y.; Cheng, Z.; Qiu, X.; Fang, Y.; Zhang, Y.; Liu, Z. Quasi-freestanding monolayer heterostructure of graphene and hexagonal boron nitride on Ir(111) with a zigzag boundary. *Nano Lett.* **2014**, *14*, 6342−6347.
(40) Mortazavi, B.; Fan, Z.; Pereira, L. F. C.; Harju, A.; Rabczuk, T. Amorphized graphene: A stiff material with low thermal conductivity. *Carbon* **2016**, *103*, 318−326.
(41) Toh, C.-T.; Zhang, H.; Lin, J.; Mayorov, A. S.; Wang, Y.-P.; Orofeo, C. M.; Ferry, D. B.; Andersen, H.; Kakenov, N.; Guo, Z.; Abidi, I. H.; Sims, H.; Suenaga, K.; Pantelides, S. T.; Özyilmaz, B. Synthesis and properties of free-standing monolayer amorphous carbon. *Nature* **2020**, *577*, 199−203.
(42) Wegner, W.; Fijalkowski, K. J.; Grochala, W. A low temperature pyrolytic route to amorphous quasi-hexagonal boron nitride from hydrogen rich (NH4)3Mg(BH4)5. *Dalton Trans* **2020**, *49*, 336−342.
(43) Hong, S.; et al. Ultralow-dielectric-constant amorphous boron nitride. *Nature* **2020**, *582*, 511−514.
(44) Fan, Z.; Chen, W.; Vierimaa, V.; Harju, A. Efficient molecular dynamics simulations with many-body potentials on graphics processing units. *Comput. Phys. Commun.* **2017**, *218*, 10−16.
(45) Fan, Z.; Siro, T.; Harju, A. Accelerated molecular dynamics force evaluation on graphics processing units for thermal conductivity calculations. *Comput. Phys. Commun.* **2013**, *184*, 1414−1425.
(46) Plimpton, S. Fast Parallel Algorithms for Short-Range Molecular Dynamics. *J. Comput. Phys.* **1995**, *117*, 1−19.
(47) Boone, P.; Babaei, H.; Wilmer, C. E. Heat Flux for Many-Body Interactions: Corrections to LAMMPS. *J. Chem. Theory Comput.* **2019**, *15*, 5579−5587.
(48) Fan, Z.; Pereira, L. F. C.; Wang, H.-Q.; Zheng, J.-C.; Donadio, D.; Harju, A. Force and heat current formulas for many-body potentials in molecular dynamics simulations with applications to thermal conductivity calculations. *Phys. Rev. B: Condens. Matter Mater. Phys.* **2015**, *92*, 094301.
(49) Surblys, D.; Matsubara, H.; Kikugawa, G.; Ohara, T. Application of atomic stress to compute heat flux via molecular dynamics for systems with many-body interactions. *Phys. Rev. E: Stat. Phys., Plasmas, Fluids, Relat. Interdiscip. Top.* **2019**, *99*, 051301.
(50) Kınacı, A.; Haskins, J. B.; Sevik, C.; Cagın, T. Thermal conductivity of BN-C nanostructures. *Phys. Rev. B: Condens. Matter Mater. Phys.* **2012**, *86*, 115410.
(51) Dhar, A. Heat transport in low-dimensional systems. *Adv. Phys.* **2008**, *57*, 457−537.
(52) Nosé, S. A unified formulation of the constant temperature molecular dynamics methods. *J. Chem. Phys.* **1984**, *81*, 511−519.
(53) Hoover, W. G. Canonical dynamics: Equilibrium phase-space distributions. *Phys. Rev. A: At., Mol., Opt. Phys.* **1985**, *31*, 1695−1697.
(54) Bussi, G.; Donadio, D.; Parrinello, M. Canonical sampling through velocity rescaling. *J. Chem. Phys.* **2007**, *126*, 014101.
(55) Li, Z.; Xiong, S.; Sievers, C.; Hu, Y.; Fan, Z.; Wei, N.; Bao, H.; Chen, S.; Donadio, D.; Ala-Nissila, T. Influence of thermostatting on nonequilibrium molecular dynamics simulations of heat conduction in solids. *J. Chem. Phys.* **2019**, *151*, 234105.
(56) CHEN, J.; ZHANG, G.; LI, B. Molecular Dynamics Simulations of Heat Conduction in Nanostructures: Effect of Heat Bath. *J. Phys. Soc. Jpn.* **2010**, *79*, 074604.
(57) Wu, X.; Han, Q. Thermal conductivity of defective graphene: an efficient molecular dynamics study based on graphics processing units. *Nanotechnology* **2020**, *31*, 215708.
(58) Wu, X.; Han, Q. Thermal conductivity of monolayer hexagonal boron nitride: From defective to amorphous. *Comput. Mater. Sci.* **2020**, *184*, 109938.
(59) Gao, Y.; Xu, B. Controllable Interface Junction, In-Plane Heterostructures Capable of Mechanically Mediating On-Demand Asymmetry of Thermal Transports. *ACS Appl. Mater. Interfaces* **2017**, *9*, 34506−34517.
(60) Loh, G.; Teo, E.; Tay, B. Phonon localization around vacancies in graphene nanoribbons. *Diamond Relat. Mater.* **2012**, *23*, 88−92.

https://dx.doi.org/10.1021/acs.jpcc.0c10387
J. Phys. Chem. C 2021, 125, 2748−2760